

LETTER TO THE EDITOR

Runaway BN supergiant star HD 93840: Progenitor of an imminent core-collapse supernova above the Galactic plane

D. Weßmayer¹, M. A. Urbaneja¹, K. Butler², and N. Przybilla¹

¹ Universität Innsbruck, Institut für Astro- und Teilchenphysik, Technikerstr. 25/8, 6020 Innsbruck, Austria
e-mail: david.wessmayer@uibk.ac.at ; norbert.przybilla@uibk.ac.at

² Ludwig-Maximilians-Universität München, Universitätssternwarte, Scheinerstr. 1, 81679 München, Germany

Received ; accepted

ABSTRACT

We present a quantitative spectral analysis of the extreme nitrogen-enhanced supergiant HD 93840 (BN1 Ib) at an intermediate galactic latitude. Based on an optical high-resolution spectrum and complementary ultraviolet and infrared (spectro-)photometry, in addition to *Gaia* data, we carried out a full characterisation of the star's properties. We used both hydrostatic and unified (photosphere+wind) model atmospheres that account for deviations from local thermodynamic equilibrium. A highly unusual surface CNO-mixing signature and a marked stellar overluminosity compared to the mass imply a binary channel for the star's past evolution. The kinematics shows that it has reached its current position above the Galactic plane as a runaway star, likely ejected by the supernova explosion of its former companion star. Its current bulk composition, with a notably increased mean molecular weight due to core He- and progressed shell H-burning, suggests an advanced evolutionary stage. It is poised to yield a rare core-collapse supernova of a blue supergiant about ten OB star population scale heights above the Galactic disk relatively soon, contributing to the metal enrichment of the circumgalactic medium.

Key words. Stars: abundances – Stars: atmospheres – Stars: evolution – Stars: fundamental parameters – supergiants

1. Introduction

Core-collapse supernovae (ccSN) from massive stars ($M \gtrsim 8 M_{\odot}$) play an important role in the cosmic matter cycle by generating metals and injecting them into the interstellar medium (ISM) rapidly on cosmic timescales. As massive stars are formed in clusters and OB associations, the collective effects of multiple spatially and temporally ($\sim 10^7$ yr) close ccSN lead to the formation of superbubbles in the ISM and to a breakout of hot gas into the galactic halo via galactic chimneys (e.g. Normandeau et al. 1996). This 'galactic fountain' model also leads to a distribution of metals into the circumgalactic environment. After some retention time ($\sim 10^8$ yr), these metals fall back onto the galactic disk and mix with the ISM over large distances (Tenorio-Tagle 1996).

Individual ccSNe may contribute to this via in situ injections of metals high above the galactic plane. These may stem from the massive members among the runaway stars (e.g. Silva & Napiwotzki 2011) or from massive hyper-runaway (e.g. Przybilla et al. 2008b) or hypervelocity stars (e.g. Przybilla et al. 2008c). In particular, the latter two may potentially explain the presence of SN remnants at large distances from the galactic plane (Filipović et al. 2022), apart from SNe Ia. The unhindered expansion of such SNe may contribute to the metallicity buildup of the intergalactic medium. The massive stars observed away from the Galactic disk are typically early B-type main-sequence and giant stars because of lifetime considerations. The binary fraction of runaway stars is significantly suppressed compared to the normal OB-star population (Gies & Bolton 1986). As a consequence, from a naive point of view, the majority of these stars should result in SNe II-P from red supergiant progenitors (Smartt 2009).

Up to now, the blue supergiant HD 93840 at intermediate galactic latitude ($b = +11.1^{\circ}$) has mostly attracted interest as a distant but nonetheless relatively bright ($V = 7.76$) background source for studies of the ISM above the Galactic plane. A wide range of studies in the optical and with International Ultraviolet Explorer (IUE, e.g. Savage & Massa 1987), Orbiting and Retrievable Far and Extreme Ultraviolet Spectrometer (ORFEUS, e.g. Widmann et al. 1998), and Far Ultraviolet Spectroscopic Explorer (e.g. Dixon et al. 2006) were conducted in this context. However, the supergiant itself has so far been of limited interest. After an initial report of it being overabundant in nitrogen from its UV spectrum (Savage & Massa 1987), it was confirmed as an extreme N-enhanced supergiant and optically classified as BN1 Ib by Walborn et al. (1990). Massa et al. (1991) derived surface carbon to nitrogen abundances of 1:10 from a differential (model-atmosphere independent) analysis of the UV wind lines of HD 93840, whereas the oxygen abundance appeared to be normal. They concluded that the photospheric material was only once shortly exposed to CN-burning, avoiding the slower modification by the ON-cycle. A single analysis with a modern model atmosphere code provided limited information (Fraser et al. 2010), as seen in Table 1. Here, we present a comprehensive analysis that shows that HD 93840 is far more interesting beyond what is known so far, constituting a unique highly-evolved and markedly overluminous runaway star that will likely explode in a rare ccSN of a blue supergiant within a relatively short timescale and located well above the Galactic plane.

arXiv:2407.01037v1 [astro-ph.SR] 1 Jul 2024

2. Observational data

Our analysis is based on two spectra of HD 93840, observed consecutively in the night of 24 April 2005 with the Fibrefed Extended Range Optical Spectrograph (FEROS, [Kaufer et al. 1999](#)) on the Max-Planck-Gesellschaft/European Southern Observatory (ESO) 2.2 m telescope at La Silla in Chile. The phase 3 data, which were downloaded from the ESO Science Portal¹, cover a useful wavelength range from about 3700 to 9200 Å at a resolving power $R = \lambda/\Delta\lambda \approx 48\,000$. The spectra were normalised by fitting a spline function through carefully selected continuum points and co-added after verification of the absence of any significant radial velocity shift, resulting in a signal-to-noise ratio of $S/N = 425$ per pixel, measured at 5585 Å.

Various sources of (spectro-)photometric data were considered in this work. In the UV, we employed spectra taken with the Tübingen Echelle Spectrograph (TUES²) on board ORFEUS-SPAS II ([Barnstedt et al. 1999](#)). Additionally, we used high-dispersion, large-aperture spectra (data IDs SWP49711 and LWP27124) taken by IUE³. We also adopted UV-photometry from the Belgian/UK Ultraviolet Sky Survey Telescope (S2/68, [Thompson et al. 1995](#)) on board the European Space Research Organisation TD1 satellite. In the optical, we considered Johnson *UBV* magnitudes ([Mermilliod 1997](#)) as well as low-resolution spectra of *Gaia* Data Release 3 (DR3, [Gaia Collaboration et al. 2016](#); [Gaia Collaboration 2022](#)). Finally, in the IR wavelength range, we employed 2MASS *JHK* magnitudes ([Cutri et al. 2003](#)) and Wide-Field Infrared Survey Explorer (WISE) photometry ([Cutri et al. 2021](#)).

3. Analysis methodology

Modelling the photospheric spectra of early B-type supergiants requires the consideration of deviations from local thermodynamic equilibrium (so-called non-LTE effects) and (in cases of very high luminosity) an explicit treatment of the stellar wind and spherical extension. While HD 93840 at luminosity class Ib is clearly not highly luminous, we nevertheless adopted two independent modelling approaches for verification purposes.

In a hybrid non-LTE approach, model atmospheres were calculated with ATLAS12 ([Kurucz 2005](#)) as line-blanketed, plane-parallel, homogeneous, and hydrostatic structures in LTE. This provided the basis for non-LTE line-formation calculations carried out with updated and extended versions of DETAIL and SURFACE ([Giddings 1981](#); [Butler & Giddings 1985](#)) and state-of-the-art model atoms. Grids of synthetic spectra were calculated and matched to the observations using χ^2 -minimisation, employing the Spectral Plotting and Analysis Suite (SPAS, [Hirsch 2009](#)). Multiple spectroscopic indicators were utilised to provide tight constraints on the atmospheric parameters. For details of the analysis procedure, we refer to [Weßmayer et al. \(2022; 2023, henceforth Papers I & II\)](#) and we also include a brief summary in Appendix A. The analysis technique based on the modelling via ATLAS12 + DETAIL + SURFACE (abbreviated as ADS henceforth) was shown to be applicable to a wide range of massive stars, that is, early B- ([Nieva & Przybilla 2007; 2012](#)) and late O-type main-sequence stars ([Aschenbrenner et al. 2023](#)), as well as BA-type supergiants ([Przybilla et al. 2006](#); [Firnstein & Przybilla 2012, Papers I, II](#)).

As a second option, unified (wind+photosphere) non-LTE model atmospheres were computed with FASTWIND ([Puls et al.](#)

Table 1. Atmospheric and stellar parameters of HD 93840.

General information:			
Sp. Type	BN1 Ib	ϖ (mas) ^a	0.3604 ± 0.0348
v_{rad} (km s ⁻¹)	-8.1 ± 0.5	μ_{α} (mas yr ⁻¹) ^b	-5.767 ± 0.03
d (kpc) ^c	~ 2.6 to ~ 2.8	μ_{δ} (mas yr ⁻¹) ^b	5.033 ± 0.03
V (mag) ^d	7.761 ± 0.013	$B - V$ (mag) ^d	-0.048 ± 0.008
Stellar parameters and elemental abundances:			
	ADS ^e	FASTWIND ^f	TLUSTY ^g
T_{eff} (kK)	21.8 ± 0.3	$23.1^{+0.9}_{-1.0}$	20.9 ± 1.0
$\log g$ (cgs)	3.00 ± 0.05	$2.90^{+0.08}_{-0.1}$	2.75 ± 0.2
ξ (km s ⁻¹)	13 ± 2	16 ± 3	15 ± 3
$v \sin i$ (km s ⁻¹)	68 ± 3	68	58 ± 3
ζ (km s ⁻¹)	65 ± 5	65	68 ± 4
$\varepsilon(\text{He})$	$11.06^{+0.07}_{-0.09}$	$11.26^{+0.18}_{-0.22}$...
$\varepsilon(\text{C})$	7.25 ± 0.09	$7.29^{+0.18}_{-0.16}$...
$\varepsilon(\text{N})$	8.59 ± 0.08	$8.53^{+0.10}_{-0.09}$	8.37 ± 0.2
$\varepsilon(\text{O})$	8.42 ± 0.05	$8.37^{+0.11}_{-0.10}$...
$\varepsilon(\text{Ne})$	8.10 ± 0.07
$\varepsilon(\text{Mg})$	7.40 ± 0.05	$7.44^{+0.13}_{-0.12}$...
$\varepsilon(\text{Al})$	6.24 ± 0.08
$\varepsilon(\text{Si})$	7.63 ± 0.08	$7.33^{+0.12}_{-0.11}$...
$\varepsilon(\text{S})$	7.32 ± 0.05
$\varepsilon(\text{Ar})$	6.61 ± 0.08
$\varepsilon(\text{Fe})$	7.33 ± 0.08
Z	0.011 ± 0.002
R_V	2.9 ± 0.1	2.95 ± 0.35	...
$E(B - V)$ (mag)	0.21 ± 0.03	0.19 ± 0.02	...
M_V (mag)	-4.82 to -5.20
M_{bol} (mag)	-6.85 to -7.23
M/M_{\odot}	7.8 to 11.0	...	23 ± 5
R/R_{\odot}	14 to 17
$\log L/L_{\odot}$	4.63 to 4.79
$\log \tau/\text{yr}$	>7.10

Notes. Uncertainties are 1σ -standard deviations, except where noted otherwise. ^(a) [Gaia Collaboration \(2022\)](#) ^(b) Accounting for magnitude-dependent systematics of *Gaia* EDR3 data according to [Cantat-Gaudin & Brandt \(2021\)](#). ^(c) Most likely full range, see Appendix B. ^(d) [Mermilliod \(1997\)](#) ^(e) Based on the ATLAS12+DETAIL+SURFACE (ADS) solution. ^(f) Derived using FASTWIND. ^(g) [Fraser et al. \(2010\)](#). For the fundamental parameters full ranges based on the likely distance interval are given.

2005; 2020), which accounts for non-LTE line blanketing, mass outflow, and spherical geometry. The code has been extensively used for the analysis of B-type supergiants in the Milky Way (e.g. [Herrero et al. 2022](#)) as well as in other galaxies (e.g. [Urbaneja et al. 2005; 2017](#); [Kudritzki et al. 2016](#)).

The interstellar sightline towards HD 93840 was characterised using the mean extinction law of [Fitzpatrick \(1999\)](#). For this, the spectral energy distribution (SED) of the ATLAS model was reddened and fitted to the observed (spectro-)photometry for the two parameters of colour excess $E(B - V)$ and total-to-selective extinction $R_V = A_V/E(B - V)$. The interstellar extinction A_V was then determined as the product of the two values.

Once the atmospheric parameters and the interstellar extinction are determined, the fundamental stellar parameters depend only on the distance. Various values may be employed in view of the different bias corrections proposed for the *Gaia* measurements, the spectroscopic distance may be adopted. Further constraints on the distance, based on the runaway nature of HD 93840 and its advanced evolutionary state, may be made (this is summarised in Appendix B). A fixed distance constrains the absolute visual magnitude, M_V , and with aid of the ATLAS model bolometric correction the absolute bolometric magnitude, M_{bol} . This can be converted into luminosity, L , which provides

¹ <https://archive.eso.org/scienceportal/home>

² <https://archive.stsci.edu/tues/>

³ <https://archive.stsci.edu/iue/>

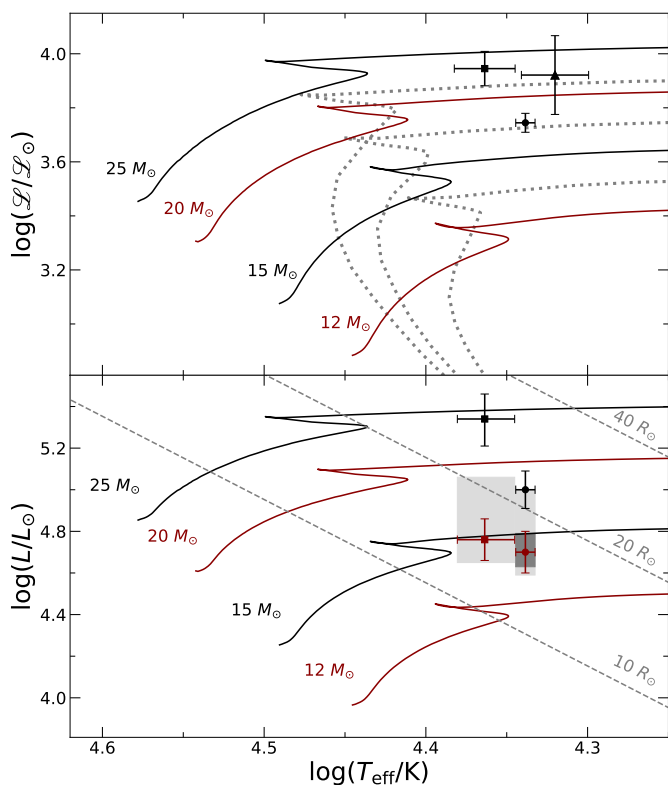


Fig. 1. Location of HD 93840 in two diagnostic diagrams, the sHRD (upper panel) and the HRD (lower panel). Parameters derived via Ads (dots), FASTWIND (squares), and TLUSTY (triangle) considering the spectroscopic and *Gaia*-based distances (i.e. d_{spec} and $d_{\text{Gaia}}^{\text{MA,EB}}$, see Appendix B), are depicted as black and red symbols, respectively. The lightgrey boxes span the parameter range obtained when accounting in addition to parallax bias according to Maíz Apellániz (2022), while the darkgrey box represents the finally adopted solution from Table 1. For comparison, loci of evolution tracks for stars rotating at $\Omega_{\text{rot}} = 0.568 \Omega_{\text{crit}}$ (Ekström et al. 2012) are indicated for various zero-age main-sequence (ZAMS) masses. Isochrones for the model grid, corresponding to ages of $\log \tau_{\text{evol}} \in \{6.95, 7.05, 7.20\}$ are shown as dotted lines in the upper panel (with age increasing from top to bottom). Error bars indicate 1σ uncertainty ranges. See the text for a discussion.

the stellar radius, R , for a given T_{eff} . Finally, from R and $\log g$, we can calculate the stellar mass, M . Usually, the stellar age, τ , can be determined from isochrones, which is inappropriate in this case, as the star’s evolution is not described well by the associated evolution tracks. Instead, a lower age limit is derived from the flight time from the Galactic mid-plane to the current location of HD 93840 above the disk (see Appendix C for details).

4. Results

All results from the quantitative analysis based on Ads and FASTWIND, plus the data obtained from the use of the TLUSTY code by Fraser et al. (2010) are summarised in Table 1. Overall, there is agreement seen among the derived atmospheric parameters of the three solutions within the mutual error bars, with the TLUSTY analysis tending to find a lower T_{eff} , whereas the FASTWIND solution indicates a higher T_{eff} (the latter follows a general trend, see Papers I & II). Line broadening parameters due to rotation and macroturbulence also agree well, except for a slightly smaller $v \sin i$ -value in the TLUSTY solution. The trend in the microturbulent velocity found in the Ads solution is towards smaller values than in the other solutions, in accordance with the find-

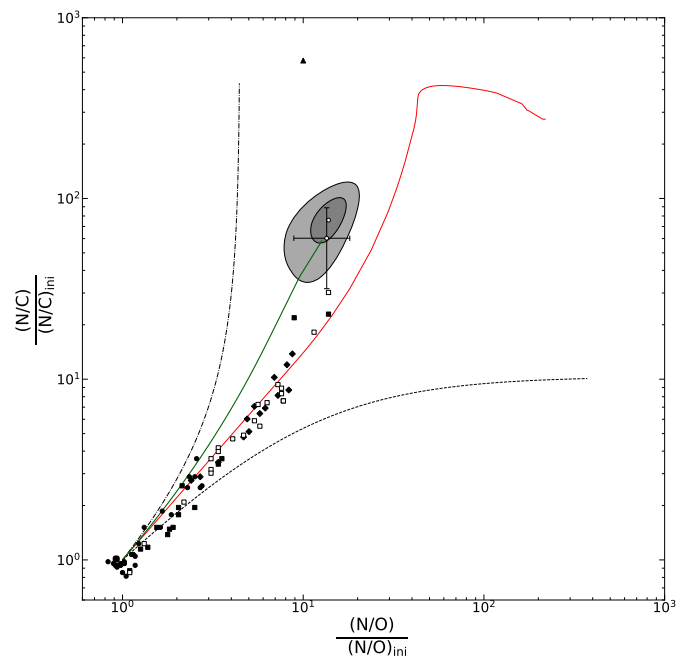


Fig. 2. Nitrogen-to-carbon ratio vs. nitrogen-to-oxygen ratio, normalised to initial values. The mixing ratios derived for HD 93840 are depicted as open dots with grey 1σ and 2σ uncertainty regions (Ads) and with error bars depicting the 1σ uncertainty (FASTWIND). Objects from our previous work are indicated: B-type main-sequence stars (Nieva & Simón-Díaz 2011; Nieva & Przybilla 2012, black dots), late O-type main-sequence stars (Aschenbrenner et al. 2023, black squares), BA-type supergiants (Przybilla et al. 2010, black diamonds), B supergiants (Paper I & II, open squares), and the stripped CN-cycled core γ Columbae (Irrgang et al. 2022, black triangle). For comparison, the development of the surface CNO abundances is shown for a $25 M_{\odot}$, $\Omega_{\text{rot}} = 0.568 \Omega_{\text{crit}}$ model (Ekström et al. 2012, red) and for a $15 M_{\odot}$, $\Omega_{\text{rot}} = 0.95 \Omega_{\text{crit}}$ model (Georgy et al. 2013, green line). The dashed and dash-dotted lines depict the analytical boundaries for the ON- and CN-cycle, respectively. A discussion is provided below.

ings of Papers I & II. This has consequences for the derivation of metal abundances which should be lower at higher ξ -values, in particular for chemical species where the abundance determination mostly relies on stronger lines (e.g. for silicon). This is exactly what we found here. The restricted set of elemental abundances derived using FASTWIND is due to the lack of detailed model atoms, and elemental abundances besides those of nitrogen were not investigated by Fraser et al. (2010). We mostly concentrate on the Ads solution for further interpretation, because of the smaller uncertainties that arise from the use of more complex model atoms and the consideration of a larger number of observational constraints in the spectroscopic analysis than employed in the other approaches.

The comparison of our final Ads and FASTWIND synthetic spectra with the full observations is shown in Figs. A.1 to A.9. Overall, an excellent fit was achieved, implying that the detailed photospheric stratification is well-matched by the models (see Appendix A for a further discussion). A high level of quality was also achieved for the SED fit from ~ 0.1 to $20 \mu\text{m}$ as shown in Fig. A.10. Therefore, the global energy output of the star was also reliably reproduced (see also Appendix A for further details).

The position of HD 93840 in the spectroscopic Hertzsprung-Russell diagram (sHRD, $\log L/L_{\odot}$ vs. $\log T_{\text{eff}}$, $L = T_{\text{eff}}^4/g$) and the classical HRD is shown in Fig. 1. The differences in the at-

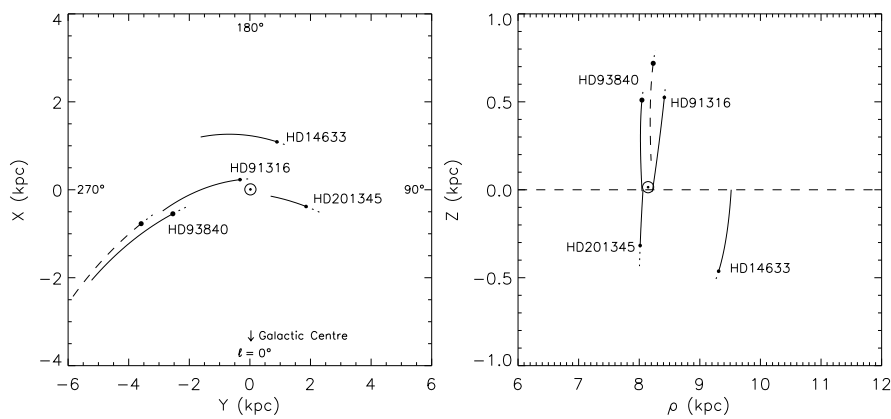


Fig. 3. Kinematics of HD 93840 (full line: adopting the *Gaia*-based distance $d_{\text{Gaia}}^{\text{MA,EB}}$, see Appendix B; dashed: spectroscopic distance d_{spec}) in the Galactic potential, together with several other runaway stars from our previous work. Galactic Cartesian coordinates XYZ are employed, with the origin shifted to the position of the Sun; ρ is the galactocentric distance. Displayed here: the Galactic plane projection (left panel) and the movement in the meridional plane (right panel). The dots mark the current positions and the orbits are traced back for the stellar age (full lines) and 2 Myr into the future (dotted lines). See the text for a discussion.

mospheric parameters, which agree well overall, become amplified by the combination into \mathcal{L} , such that the three solutions from Table 1 span quite a range in the parameter space of the sHRD. When comparing the positions of the Afs and the FASTWIND solutions in the sHRD and those based on the spectroscopic distance in the HRD, a good agreement is found. However, the *Gaia*-based luminosities (the two red symbols and grey boxes, see the discussion in Appendix B) are notably lower, but they mutually agree much better – except for the aforementioned shift in T_{eff} .

The determination of the mass and stellar age by comparison with evolution tracks and isochrones in the sHRD apparently has the advantage that only knowledge of T_{eff} and $\log g$ is required. However, there is a catch: the evolutionary tracks, such as the ones for rotating stars by Ekström et al. (2012) used here, have to come close to the real evolutionary scenario for the investigated star. That is, the star is a normally evolving single star or an object in a binary that has not yet experienced interaction. Usually, good agreement between the spectroscopic and *Gaia* parallax-based distances has been achieved in our previous studies of massive stars (see e.g. Papers I & II, Aschenbrenner et al. 2023). In that case, the positions of a star relative to the evolutionary tracks in the sHRD and the HRD are similar. However, there are exceptions, as is the case for HD 93840 in the present work (and the two ON stars discussed by Aschenbrenner et al. 2023). This is because our most likely distance value of ~ 2.6 to 2.8 kpc is significantly shorter than $d_{\text{spec}} \approx 3.7$ kpc and, therefore, the luminosity, radius and mass of HD 93840 are lower. This implies that the tracks used are inappropriate to describe the evolutionary status of the star correctly. In the following, further constraints will be employed to investigate what kind of object HD 93840 really is.

5. Discussion

The usual suspects for blue stars at high galactic latitudes with supergiant characteristics are post-asymptotic giant branch stars, but such a scenario can be excluded for HD 93840 because pre-white dwarfs have masses smaller than the Chandrasekhar limit. We therefore resort to investigating the surface CNO abundances as indicators for the evolutionary status. The nitrogen-to-carbon ratio versus the nitrogen-to-oxygen ratio (normalised to initial abundances adopted from Nieva & Przybilla 2012 and the model abundance ratios normalised to their respective initial values) of HD 93840 is depicted in Fig. 2, where it is also set into the context of massive stars we previously analysed. The mixing of the surface layers with CNO-processed matter follows a tight path in the diagram (Przybilla et al. 2010; Maeder et al. 2014). One

clear outlier was recently found, namely: the stripped star γ Col, which exposes previously CN-burning layers on its surface (Irrgang et al. 2022). The mixing signature of HD 93840 also deviates from the locus of the other stars. Yet, in principle, it could be reached by a near-critically rotating single $15 M_{\odot}$ star at the end of its lifetime (adopting a model of Georgy et al. 2013 with an initial $v_{\text{rot}} = 525 \text{ km s}^{-1}$, the green line in Fig. 2), as lower-mass stars tend to have less O-depletion, due to a slower ON-cycle relative to more massive stars. However, HD 93840 would be expected to be a red supergiant from this model⁴, contrary to observation – rendering this scenario inapplicable.

The observed high mixing signature points in the right direction, however. We can compare the luminosity of HD 93840 with a normal star of the same M and T_{eff} (interpolating the models of Ekström et al. 2012) and find a notable overluminosity. The generalised mass-luminosity relationship is $L \propto M^{\alpha} \mu^{\beta}$, with $\mu = (2X + \frac{3}{4}Y + \frac{1}{2}Z)^{-1}$ being the mean molecular weight for mass fractions of hydrogen X , helium Y and the metals Z , and $\beta \approx 4$ (Kippenhahn et al. 2013). The overluminosity therefore stems from a significantly increased mean molecular weight for the bulk stellar material, from about 0.6 for a standard initial composition to about 0.88 to 1.07 at present for our most likely distance range. As the mean molecular weight of H-burning regions increases to a maximum value of 1.34 when fully converted to helium, this implies the presence of a substantial He-burning core of several solar masses (including He-burning products) and an increased He-abundance in the envelope (see Appendix B for further discussion). With such a composition the star will stay a blue supergiant throughout its remaining life that will end in a ccSN, and a binary channel for its formation is indicated (e.g. Wellstein et al. 2001).

Sometimes further information on the formation scenario can be derived from a star’s kinematics. This is the case here and in Appendix C, we offer more details on the modelling and some further discussion. The visualisation of the orbit in the disk and in the meridional plane in Fig. 3 shows that HD 93840 is a runaway star originating from the Carina-Sagittarius spiral arm in the fourth Galactic quadrant (see e.g. Pantaleoni González et al. 2021). It exhibits a peculiar velocity perpendicular to the disk, such that it could have reached its current position within about 12.5 to 12.7 Myr. Its current velocity in the Galactic Z-direction is $\sim 28 \text{ km s}^{-1}$, slowed down from a value of $\sim 48 \text{ km s}^{-1}$ at Galactic midplane crossing (the assumed point of binary breakup). We note that the second solution of HD 93840, based on the spectroscopic distance and assuming it to have evolved as a single star,

⁴ We note that single stars of such mass do not experience mass loss strong enough to shed sufficient hydrogen-rich envelope to turn into a blue supergiant.

would allow it to reach its current position within the star's lifetime when started from about 150 pc above the disk. However, we have discarded the scenario because of the other peculiarities of the star. The footpoint of HD 93840's trajectory in the disk is close to the galactocentric distance of the Sun (8.178 kpc, Gravity Collaboration et al. 2019). Thus, the metal abundances of the star should be close to cosmic abundance standard values (Przybilla et al. 2008a; Nieva & Przybilla 2012), which are representative for the present-day chemical composition of the solar vicinity. With the clear exception of CNO, this is indeed the case on the whole.

An SN ejection (Blaauw 1961) is compatible with a binary evolution scenario, but the solid angle of HD 93840 (as seen from the SN) appeared small enough to avoid any notable pollution with SN ejecta, which is rare (Przybilla et al. 2008b; Irrgang et al. 2010). In fact, this, the CNO signature, and the bulk composition of HD 93840 may be used to put further constraints on the binary evolution scenario. Usually, it is the mass accretor that enters a long-lived phase in the OB-star domain, whereas the mass-losing primary star turns into a (very) hot helium star (e.g. Wellstein et al. 2001). As the accreting secondary shows only a small overluminosity, if at all (Sen et al. 2022), such a scenario can be excluded for HD 93840.

We sketch out the following scenario: HD 93840 was the primary of a close binary system which transferred mass in a Case A scenario to its initially lower mass-companion, thus becoming a relatively long-lived He-core, that is: a (massive) sdO subdwarf star. The secondary was spun-up by the mass transfer to close to critical velocity, became rejuvenated and its evolution became faster than that of the primary; this is a situation that is encountered in early Be-star-and-sdO subdwarf systems (e.g. Wang et al. 2021). In particular, if the mass transfer became non-conservative at some point, the separation of the two stars could have grown larger. Mass transfer from the evolved secondary in an early Case B scenario (i.e. after termination of core H-burning) could then have transferred back strongly CNO-processed material to the He-core primary. The SN explosion of the secondary's core shortly after then disrupted the system, sending HD 93840 on its observed trajectory. As the chemically most-processed material was deposited on the surface, this created an inverse μ -gradient in the radiative envelope of HD 93840. Thermohaline mixing set in and led to a dilution of the initial CNO signature, similar to what would otherwise be reached by convectively mixing highly CNO-processed material from near the core with the envelope of a red supergiant. This scenario should certainly be substantiated by dedicated binary evolution calculations, however, this is beyond the scope of the present work.

Irrespective of the details of the binary scenario, with an evolutionary stage advanced well into He-burning, a He-core mass above the Chandrasekhar limit, and the high overall mean molecular weight keeping the star from evolving to red supergiant dimensions, the core-collapse of HD 93840 as a blue supergiant seems imminent within a relatively short timescale. The resulting SN explosion may share some similarities with SN1987A due to its blue supergiant progenitor (Walborn et al. 1989) as well as differences due to environment and progenitor evolution (e.g. Podsiadlowski 1992). We note that our estimated He-core mass of about 4 to 5 M_{\odot} (see Appendix B) is a bit lower than that of the SN1987A progenitor (5–7 M_{\odot} , Arnett et al. 1989), while the envelope mass of HD 93840 is significantly lower. The ccSN of HD 93840 will occur about 500 to 600 pc (i.e. about ten typical OB star population scale heights) above the Galactic mid-plane. By injecting metals into the circumgalactic medium,

it will feed the metallicity buildup of the circumgalactic medium more directly than via galactic fountains.

Acknowledgements. We express our gratitude to U. Bastian for invaluable advice regarding *Gaia* data. We also want to thank the referee for suggestions that helped to improve the paper and our second reviewer for clarifications and constructive propositions on considering parallax bias for the distance determination. D.W. and N.P. gratefully acknowledge support from the Austrian Science Fund FWF project DK-ALM, grant W1259-N27. Based on observations collected at the European Southern Observatory under ESO programmes 075.D-0103(A) and 092.C-0173(A), obtained from the European Southern Observatory Science Archive Facility with DOIs <https://doi.org/10.18727/archive/24> and <https://doi.org/10.18727/archive/50>.

References

- Allen, C. & Santillan, A. 1991, *Rev. Mexicana Astron. Astrofis.*, 22, 255
- Arnett, W. D., Bahcall, J. N., Kirshner, R. P., & Woosley, S. E. 1989, *ARA&A*, 27, 629
- Aschenbrenner, P., Przybilla, N., & Butler, K. 2023, *A&A*, 671, A36
- Bailer-Jones, C. A. L., Rybizki, J., Fousneau, M., Demleitner, M., & Andrae, R. 2021, *AJ*, 161, 147
- Barnstedt, J., Kappellmann, N., Appenzeller, I., et al. 1999, *A&AS*, 134, 561
- Blaauw, A. 1961, *Bull. Astron. Inst. Netherlands*, 15, 265
- Butler, K. & Giddings, J. R. 1985, *Newsletter of Analysis of Astronomical Spectra*, 9 (Univ. London)
- Cantat-Gaudin, T. & Brandt, T. D. 2021, *A&A*, 649, A124
- Cutri, R. M., Skrutskie, M. F., van Dyk, S., et al. 2003, *VizieR Online Data Catalog*, II/246
- Cutri, R. M., Wright, E. L., Conrow, T., et al. 2021, *VizieR Online Data Catalog*, II/328
- Dekker, H., D'Odorico, S., Kaufer, A., Delabre, B., & Kotzlowski, H. 2000, *SPIE Conf. Ser.*, 4008, 534
- Dixon, W. V. D., Sankrit, R., & Otte, B. 2006, *ApJ*, 647, 328
- Ekström, S., Georgy, C., Eggenberger, P., et al. 2012, *A&A*, 537, A146
- El-Badry, K., Rix, H.-W., & Heintz, T. M. 2021, *MNRAS*, 506, 2269
- Feast, M. W., Thackeray, A. D., & Wesselink, A. J. 1955, *MmRAS*, 67, 51
- Filipović, M. D., Payne, J. L., Alsaberi, R. Z. E., et al. 2022, *MNRAS*, 512, 265
- Firnstein, M. & Przybilla, N. 2012, *A&A*, 543, A80
- Fitzpatrick, E. L. 1999, *PASP*, 111, 63
- Flynn, C., Sekhri, R., Venville, T., et al. 2022, *MNRAS*, 509, 4276
- Fraser, M., Dufton, P. L., Hunter, I., & Ryans, R. S. I. 2010, *MNRAS*, 404, 1306
- Gaia Collaboration. 2022, *VizieR Online Data Catalog*, I/355
- Gaia Collaboration, Prusti, T., de Bruijne, J. H. J., et al. 2016, *A&A*, 595, A1
- Gaia Collaboration, Vallenari, A., Brown, A. G. A., et al. 2023, *A&A*, 674, A1
- Georgy, C., Ekström, S., Eggenberger, P., et al. 2013, *A&A*, 558, A103
- Giddings, J. R. 1981, PhD thesis, (Univ. London)
- Gies, D. R. & Bolton, C. T. 1986, *ApJS*, 61, 419
- Gravity Collaboration, Abuter, R., Amorim, A., et al. 2019, *A&A*, 625, L10
- Herrero, A., Berlanas, S. R., Gil de Paz, A., et al. 2022, *MNRAS*, 511, 3113
- Hirsch, H. A. 2009, PhD thesis, (Univ. Erlangen-Nürnberg)
- Irrgang, A., Przybilla, N., Heber, U., Nieva, M. F., & Schuh, S. 2010, *ApJ*, 711, 138
- Irrgang, A., Przybilla, N., & Meynet, G. 2022, *Nat. Astron.*, 6, 1414
- Kaufer, A., Stahl, O., Tubbesing, S., et al. 1999, *The Messenger*, 95, 8
- Kippenhahn, R., Weigert, A., & Weiss, A. 2013, *Stellar Structure and Evolution*, 2nd ed. (Springer, Berlin Heidelberg)
- Kudritzki, R. P., Castro, N., Urbaneja, M. A., et al. 2016, *ApJ*, 829, 70
- Kurucz, R. L. 2005, *Mem. Soc. Astron. Ital. Suppl.*, 8, 14
- Lindgren, L., Bastian, U., Biermann, M., et al. 2021, *A&A*, 649, A4
- Mackereth, J. T., Bovy, J., Schiavon, R. P., et al. 2017, *MNRAS*, 471, 3057
- Maeder, A., Przybilla, N., Nieva, M. F., et al. 2014, *A&A*, 565, A39
- Maíz-Apellániz, J. 2001, *AJ*, 121, 2737
- Maíz-Apellániz, J. 2022, *A&A*, 657, A130
- Maíz-Apellániz, J., Alfaro, E. J., & Sota, A. 2008, arXiv e-prints, arXiv:0804.2553
- Massa, D., Altner, B., Wynne, D., & Lamers, H. J. G. L. M. 1991, *A&A*, 242, 188
- Mermilliod, J. C. 1997, *VizieR Online Data Catalog*, 2168
- Nieva, M. F. & Przybilla, N. 2006, *ApJ*, 639, L39
- Nieva, M. F. & Przybilla, N. 2007, *A&A*, 467, 295
- Nieva, M. F. & Przybilla, N. 2012, *A&A*, 539, A143
- Nieva, M. F. & Simón-Díaz, S. 2011, *A&A*, 532, A2
- Normandeau, M., Taylor, A. R., & Dewdney, P. E. 1996, *Nature*, 380, 687
- Odenkirchen, M. & Brosche, P. 1992, *Astronomische Nachrichten*, 313, 69
- Pantaleoni González, M., R. H., & Reed, B. C. 2021, *MNRAS*, 504, 2968
- Podsiadlowski, P. 1992, *PASP*, 104, 717
- Prinja, R. K. & Massa, D. L. 2013, *A&A*, 559, A15

- Przybilla, N. & Butler, K. 2001, A&A, 379, 955
- Przybilla, N., Butler, K., Becker, S. R., & Kudritzki, R. P. 2006, A&A, 445, 1099
- Przybilla, N., Butler, K., & Kudritzki, R. P. 2001, A&A, 379, 936
- Przybilla, N., Firnstein, M., Nieva, M. F., Meynet, G., & Maeder, A. 2010, A&A, 517, A38
- Przybilla, N., Nieva, M. F., & Butler, K. 2008a, ApJ, 688, L103
- Przybilla, N., Nieva, M. F., Heber, U., & Butler, K. 2008b, ApJ, 684, L103
- Przybilla, N., Nieva, M. F., Heber, U., et al. 2008c, A&A, 480, L37
- Puls, J., Najarro, F., Sundqvist, J. O., & Sen, K. 2020, A&A, 642, A172
- Puls, J., Urbaneja, M. A., Venero, R., et al. 2005, A&A, 435, 669
- Savage, B. D. & Massa, D. 1987, ApJ, 314, 380
- Sen, K., Langer, N., Marchant, P., et al. 2022, A&A, 659, A98
- Silva, M. D. V. & Napiwotzki, R. 2011, MNRAS, 411, 2596
- Smartt, S. J. 2009, ARA&A, 47, 63
- Tenorio-Tagle, G. 1996, AJ, 111, 1641
- Thompson, G. I., Nandy, K., Jamar, C., et al. 1995, VizieR Online Data Catalog, II/59B
- Urbaneja, M. A., Herrero, A., Bresolin, F., et al. 2005, ApJ, 622, 862
- Urbaneja, M. A., Kudritzki, R. P., Gieren, W., et al. 2017, AJ, 154, 102
- Vrancken, M., Butler, K., & Becker, S. R. 1996, A&A, 311, 661
- Walborn, N. R., Fitzpatrick, E. L., & Nichols-Bohlin, J. 1990, PASP, 102, 543
- Walborn, N. R., Prevot, M. L., Prevot, L., et al. 1989, A&A, 219, 229
- Wang, L., Gies, D. R., Peters, G. J., et al. 2021, AJ, 161, 248
- Wellstein, S., Langer, N., & Braun, H. 2001, A&A, 369, 939
- Weßmayer, D., Przybilla, N., & Butler, K. 2022, A&A, 668, A92
- Weßmayer, D., Przybilla, N., Ebenbichler, A., Aschenbrenner, P., & Butler, K. 2023, A&A, 677, A175
- Widmann, H., de Boer, K. S., Richter, P., et al. 1998, A&A, 338, L1

Appendix A: Spectral analysis of HD 93840

The determination of the atmospheric parameters from the high-resolution optical spectrum proceeded as follows. Effective temperature, T_{eff} , and surface gravity, $\log g$, were established by simultaneously reproducing the Stark-broadened higher Balmer lines and ionisation equilibria of He I/II and multiple metallic species (e.g. O I/II and Si II/III/IV). The microturbulent velocity, ξ , was constrained by requiring elemental abundances to be independent of line equivalent width. Fitting individual line profiles then established the projected rotational velocity, $v \sin i$, and the macroturbulent velocity, ζ , (applying a convolution with rotational and radial-tangential profiles), and the elemental abundances, $\varepsilon(X) = \log(X/H) + 12$. The metallicity, Z , was computed from the abundances of the elements discussed here, which cover the most important chemical species.

Figures A.1 to A.9 show the comparison of the ADS and FASTWIND model fluxes with the normalised FEROS spectrum. A good match is found overall, with the ADS solution reproducing a wider range of spectral lines because more chemical species were considered compared to the FASTWIND model. We note that N III is currently missing in the suite of model atoms used with ADS, but it is considered in the FASTWIND solution.

The lower Balmer lines H γ and H β , and in particular H α , are slightly affected by the stellar wind, leading to line asymmetries and some filling-in of the line profile by wind emission. Small asymmetries due to extra blue absorption by the stellar wind have also to be noted for the two strongest He I lines $\lambda\lambda 5875$ and 6678 \AA . It turned out not to be straightforward to reproduce the wind signatures of HD 93840. While the wind terminal velocity can rather easily be determined empirically from the presence of well-developed narrow absorption components (NACs) in the strong UV resonance lines to $v_{\infty} \approx 1075 \text{ km s}^{-1}$ (Prinja & Massa 2013), it is not the case for the other wind parameters, in particular the mass-loss rate. The generation of wind emission in high-ionisation species like N V (requiring $\sim 100 \text{ eV}$ for populating the ion) – with the N V $\lambda\lambda 1238.8$ and 1242.8 \AA doublet providing the strongest P-Cygni feature in the available UV spectra – points towards X-ray production in the shocked plasma of a clumped wind. As the focus of the present work is on the photospheric and fundamental stellar properties of the star, we did not pursue this topic further within the FASTWIND modelling framework.

The wings of higher Balmer lines H δ and H ϵ are matched well, but the comparison of the models with the Paschen series should only be used for guidance, as the normalisation in this spectral region and the quality of the spectrum was complicated by telluric lines and fringing. Concerning ionisation equilibria, in particular the He I/II, O I/II, and Si II/III/IV (and for the FASTWIND solution also N II/III) lines are matched simultaneously. Perfect fits for the metal lines could in most cases be achieved by adjusting the abundances within the 1σ -uncertainties stated in Table 1, considering that systematic errors of the abundances because of uncertainties in atmospheric parameters, atomic data and continuum placement amount to about 0.1 to 0.15 dex (e.g. Przybilla et al. 2001; Przybilla & Butler 2001). Only a few spectral lines show larger deviations, which may be due to model atoms that are rather simple and have seen only minor updates of atomic data for some time, for example S II/III (Vrancken et al. 1996), or that have a history of being difficult to reproduce such as the C II $\lambda\lambda 4267$, 6578 and 6582 \AA features (Nieva & Przybilla 2006, note that the FASTWIND implementation of the model atom copes better with these features here). The reproduction of the spectrum implies that the detailed atmospheric stratification in the line-forming region is matched well by the model atmospheres.

Moreover, the models also allow the global energy output of the star from the far-UV below 1000 \AA to the thermal infrared beyond $20 \mu\text{m}$ to be reproduced. Figure A.10 shows the comparison of the reddened ATLAS model with the observed SED. A good match with small residuals overall is found, as is also the case for the FASTWIND model.

Finally, we want to mention the rich spectrum of interstellar lines present in the optical data of HD 93840 (Figs A.1 to A.9). These cover resonance lines from Na I, K I and Ca I/II, numerous diffuse interstellar bands (DIBs), and even the molecular cation CH⁺, which are also identified in the figures.

Appendix B: Distance

Even in the absence of a direct parallax measurement, one possibility to constrain the distance to a star is the determination of the so-called ‘spectroscopic distance’. Based on T_{eff} and $\log g$, the stellar ‘evolutionary’ mass was derived from a comparison with evolutionary tracks for rotating single stars (Ekström et al. 2012), and Eqn. 3 from Paper I was employed. This provided $d_{\text{spec}} = 3740 \pm 340 \text{ pc}$. The caveat in this is that the evolutionary status of the star has to be reasonably close to that indicated by the stellar evolution models.

Fortunately, the *Gaia* mission (Gaia Collaboration et al. 2016) provided a plethora of parallax measurements ϖ . In the literature, the procedure currently most frequently used for deriving distances from the published *Gaia* EDR3 parallaxes is to resort to the data provided by Bailer-Jones et al. (2021), derived from a Bayesian approach. The ‘photogeometric distance’ amounts to a (rounded) value of $d_{\text{Gaia}} = 2650_{-230}^{+240} \text{ pc}$ (uncertainties are the associated 16th and 84th percentiles) for HD 93840. An alternative distance value from the same source may be the ‘geometric distance’, rounded to $2630_{-240}^{+360} \text{ pc}$. We note that the distances provided by Bailer-Jones et al. account for the parallax zero-point correction of Lindegren et al. (2021, abbreviated as L21 in the following). These values are in excellent agreement with the inverted *Gaia* EDR3 parallax distance of $2650_{-220}^{+270} \text{ pc}$, accounting again for the L21 zero-point correction.

Yet, the question of the distance to Galactic stars even in the core region of *Gaia* measurements ($\sigma_{\varpi}/\varpi < 0.1$ for HD 93840, making this parallax very precise compared to most of the *Gaia* data) is still under debate with the refined solution of *Gaia* (E)DR3. The issues are the presence and the extent of systematic bias, namely on the parallax zero point and on the parallax uncertainty values.

First, we address the question of the zero-point bias, as this is less critical. For bright blue stars like HD 93840 the parallax zero-point correction – as determined by Maíz Apellániz (2022) on basis of blue star cluster members by tying them differentially to the cluster parallax – may bring improvements over the L21 solution. A more negative zero-point correction is indicated, by a further $\sim 0.012 \text{ mas}$. This is additionally supported by the independent work of Flynn et al. (2022) who also found a colour-dependent zero-point offset for bright blue stars of the order -0.01 mas , also based on the analysis of stars in clusters. However, the zero-point difference is small compared to the parallax uncertainty.

Work subsequent to *Gaia* EDR3 found that the published parallax uncertainties may be somewhat underestimated (see e.g. Sect. 3.3 of Gaia Collaboration et al. 2023). Using the *Gaia* EDR3 parallax, the zero-point correction of Maíz Apellániz (2022) and the formula of El-Badry et al. (2021) for the parallax uncertainty adjustment, we derive a distance to HD 93840

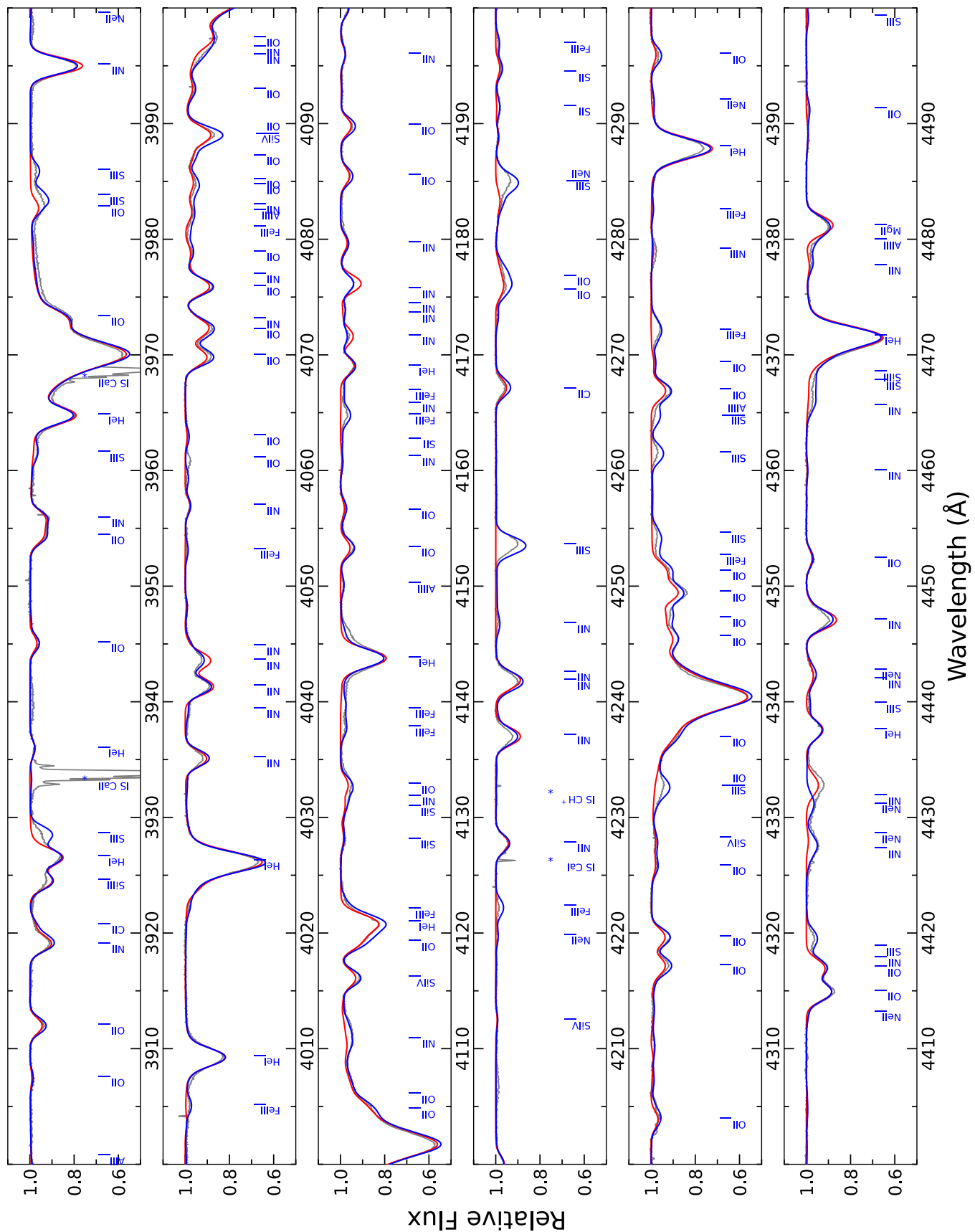


Fig. A.1. Comparison between the observed spectrum of HD 93840 (grey) and the best fitting synthetic spectra calculated with Abs (blue) and FASTWIND (red) in the wavelength range of 3900 to 4500 Å. The observed stellar spectrum was shifted to the laboratory rest frame.

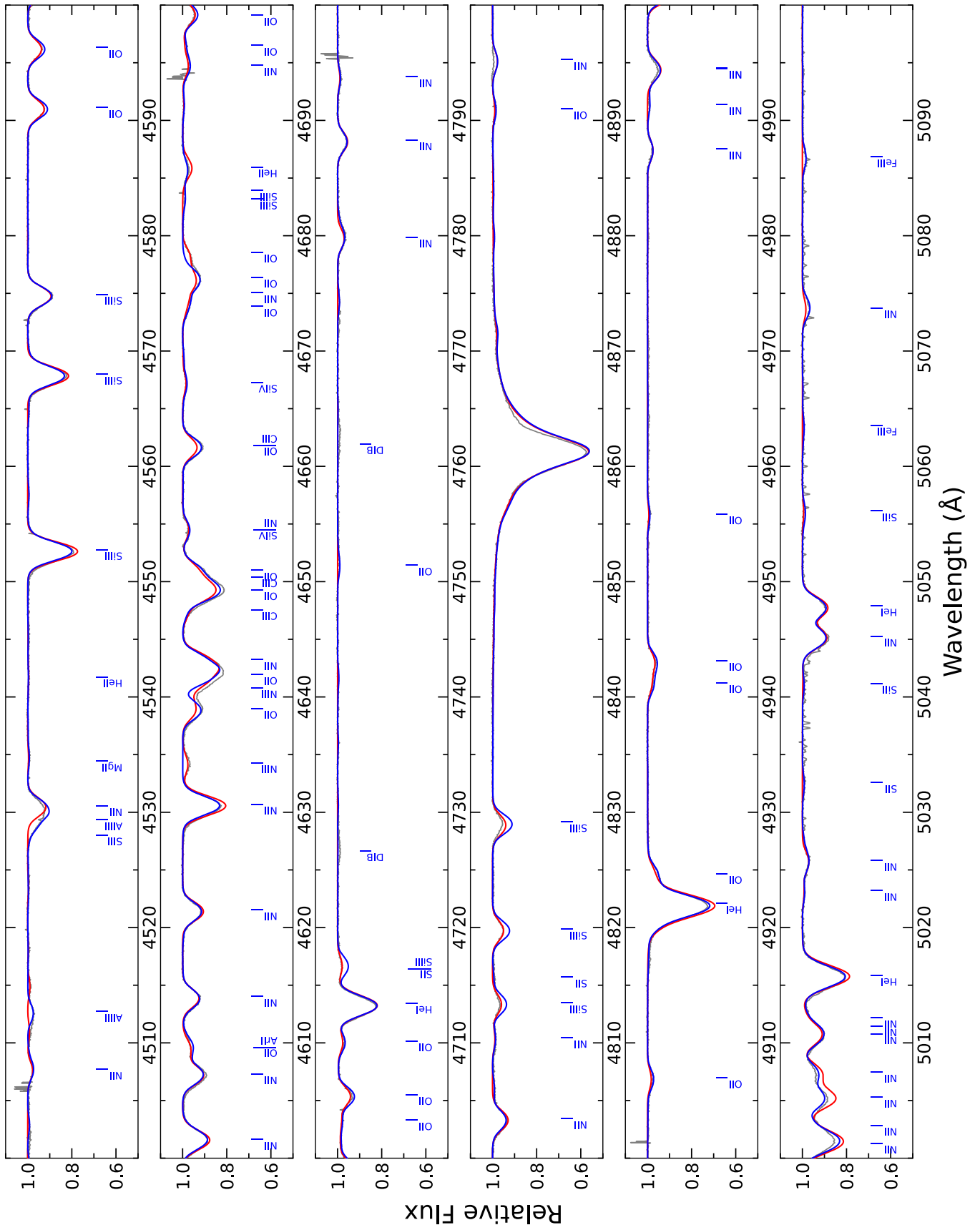


Fig. A.2. Same as Fig. A.1, but in the wavelength range 4500 to 5100 Å.

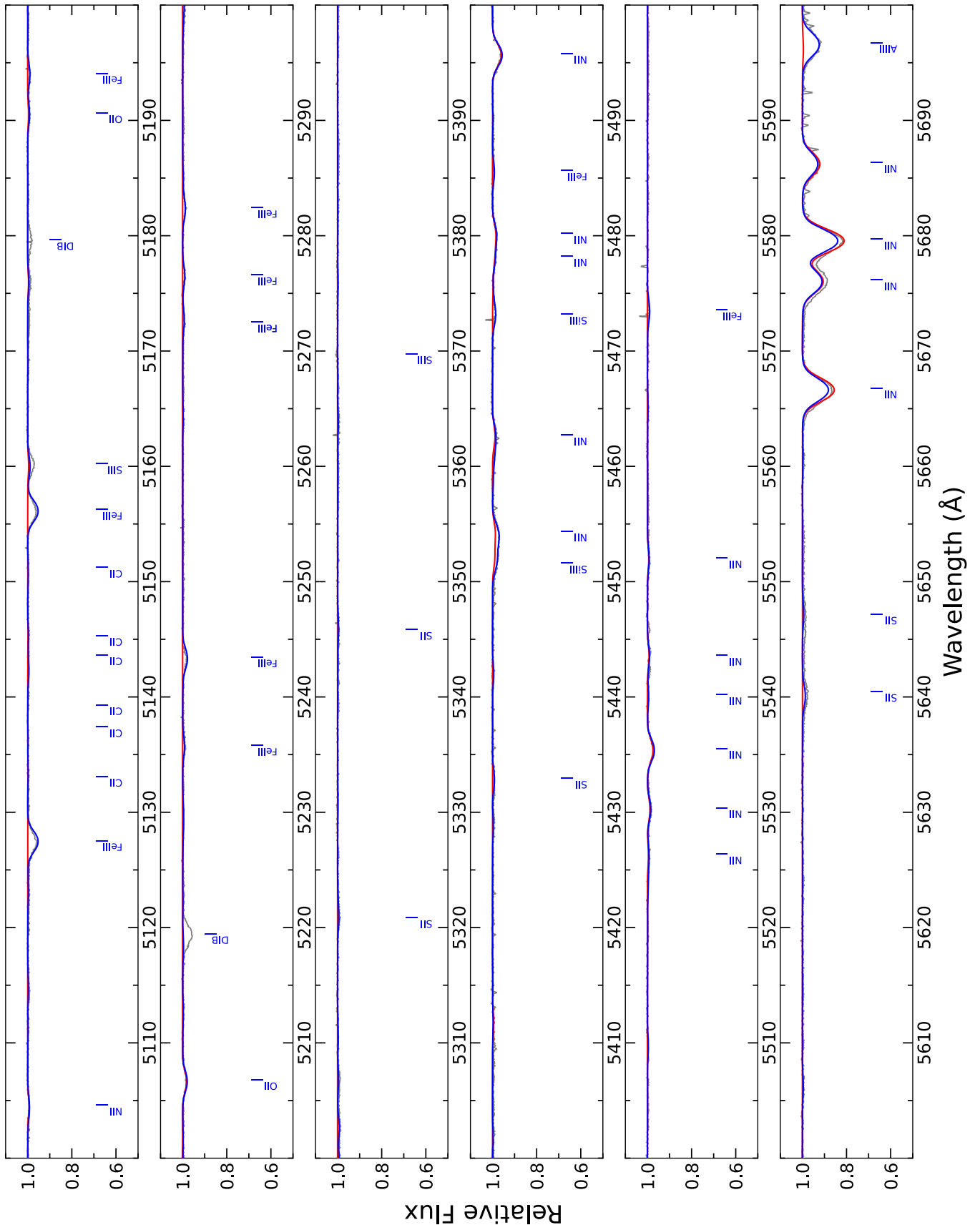


Fig. A.3. Same as Fig. A.1, but in the wavelength range 5100 to 5700 Å.

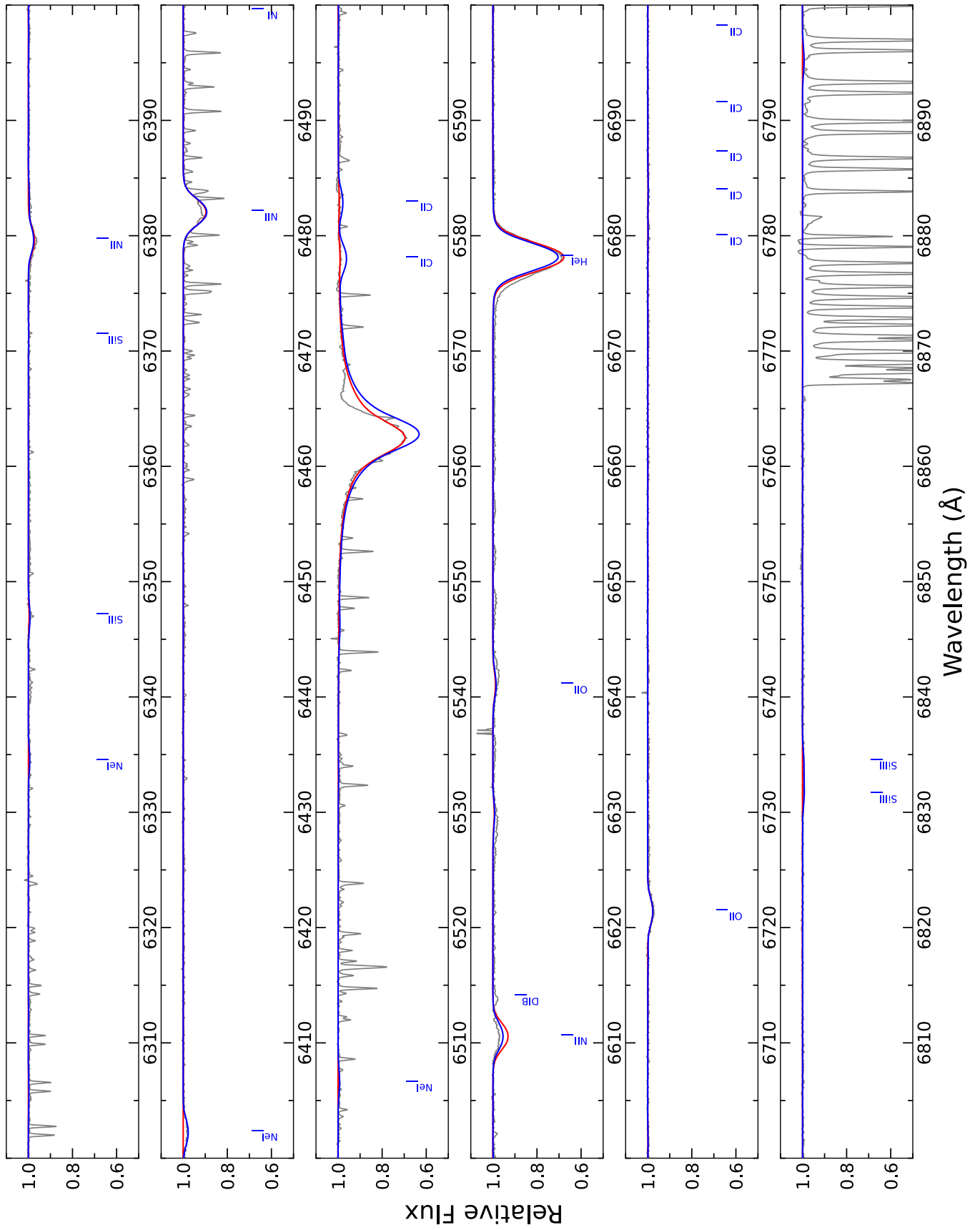


Fig. A.5. Same as Fig. A.1, but in the wavelength range 6300 to 6900 Å.

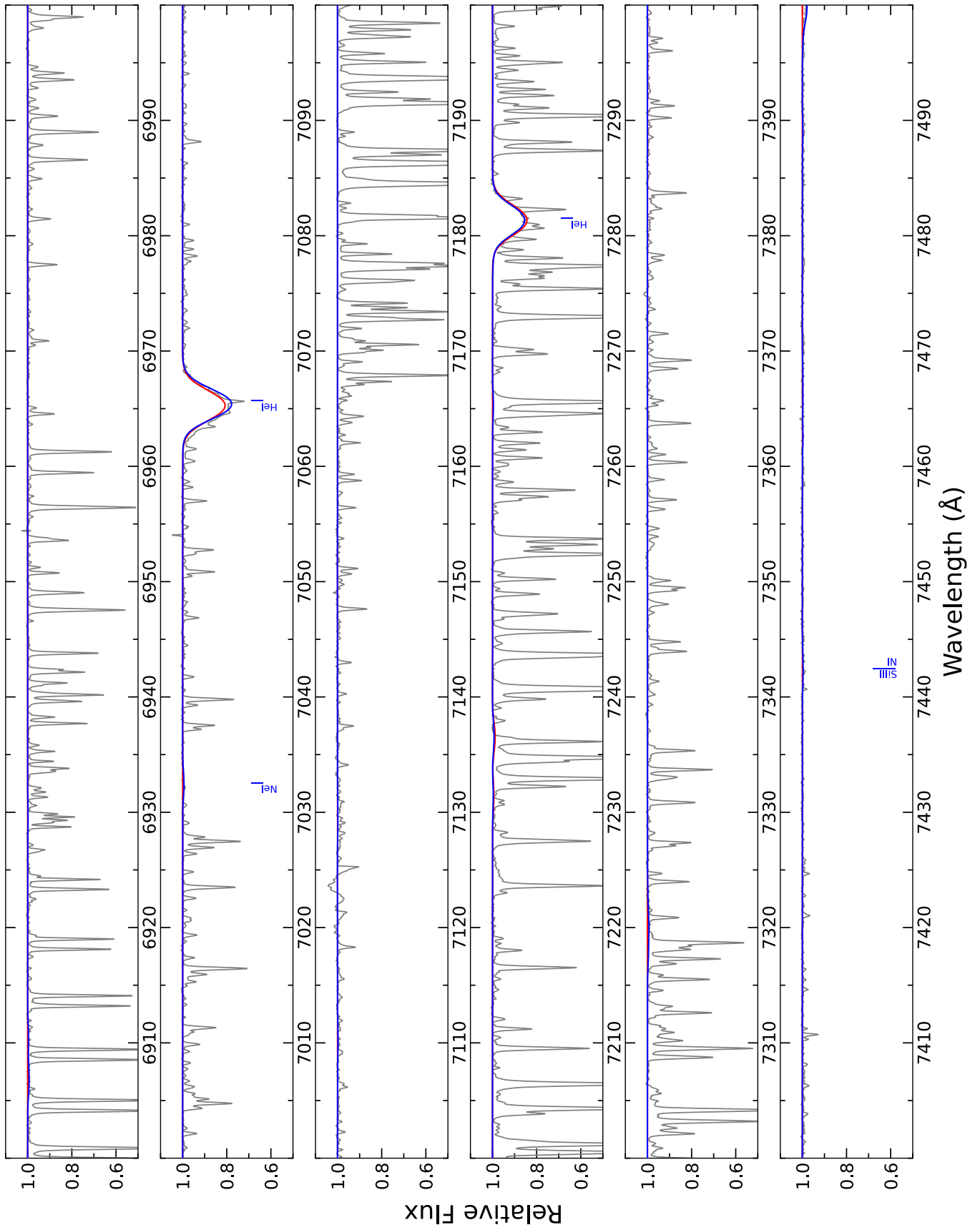


Fig. A.6. Same as Fig. A.1, but in the wavelength range 6900 to 7500 Å.

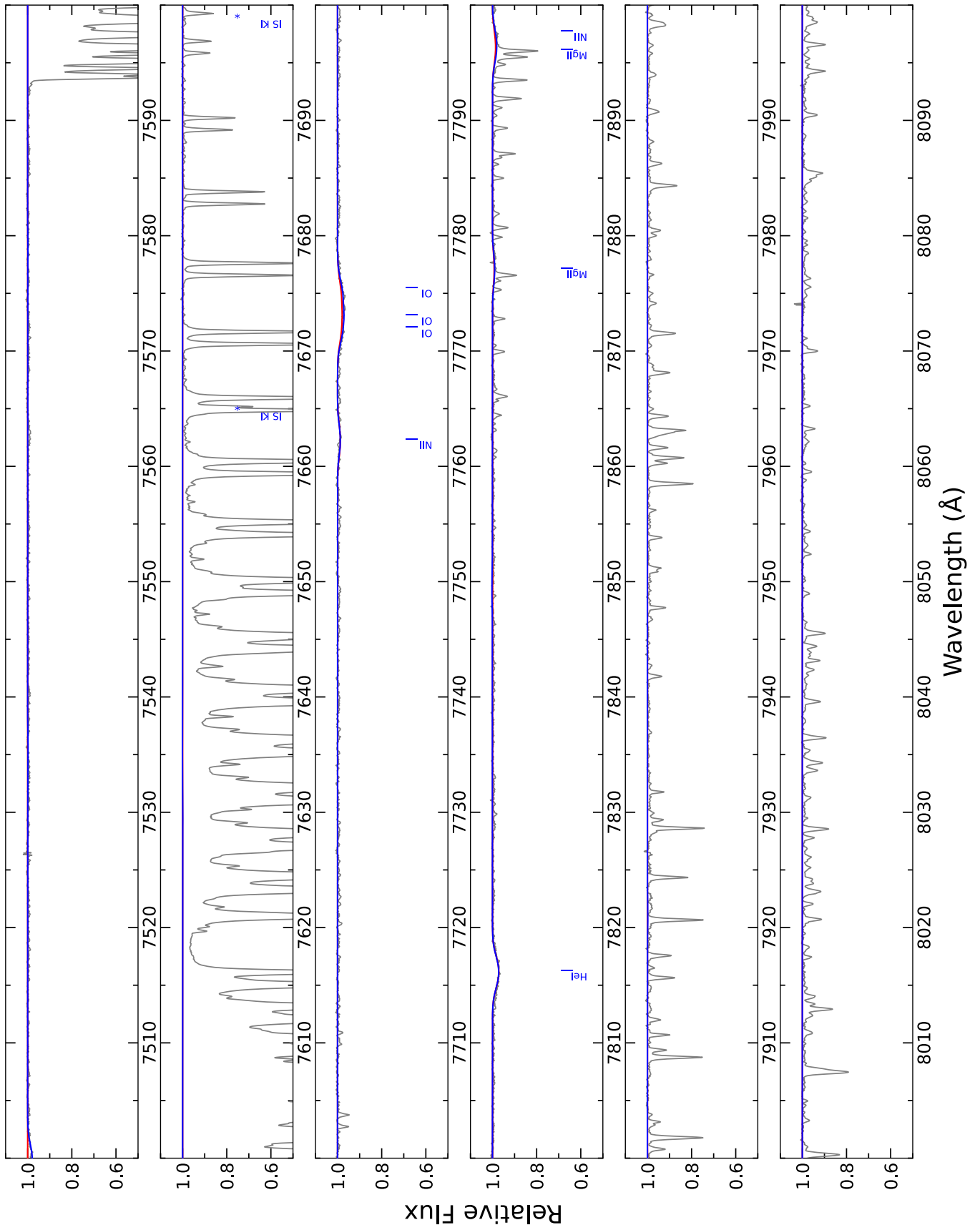


Fig. A.7. Same as Fig. A.1, but in the wavelength range 7500 to 8100 Å.

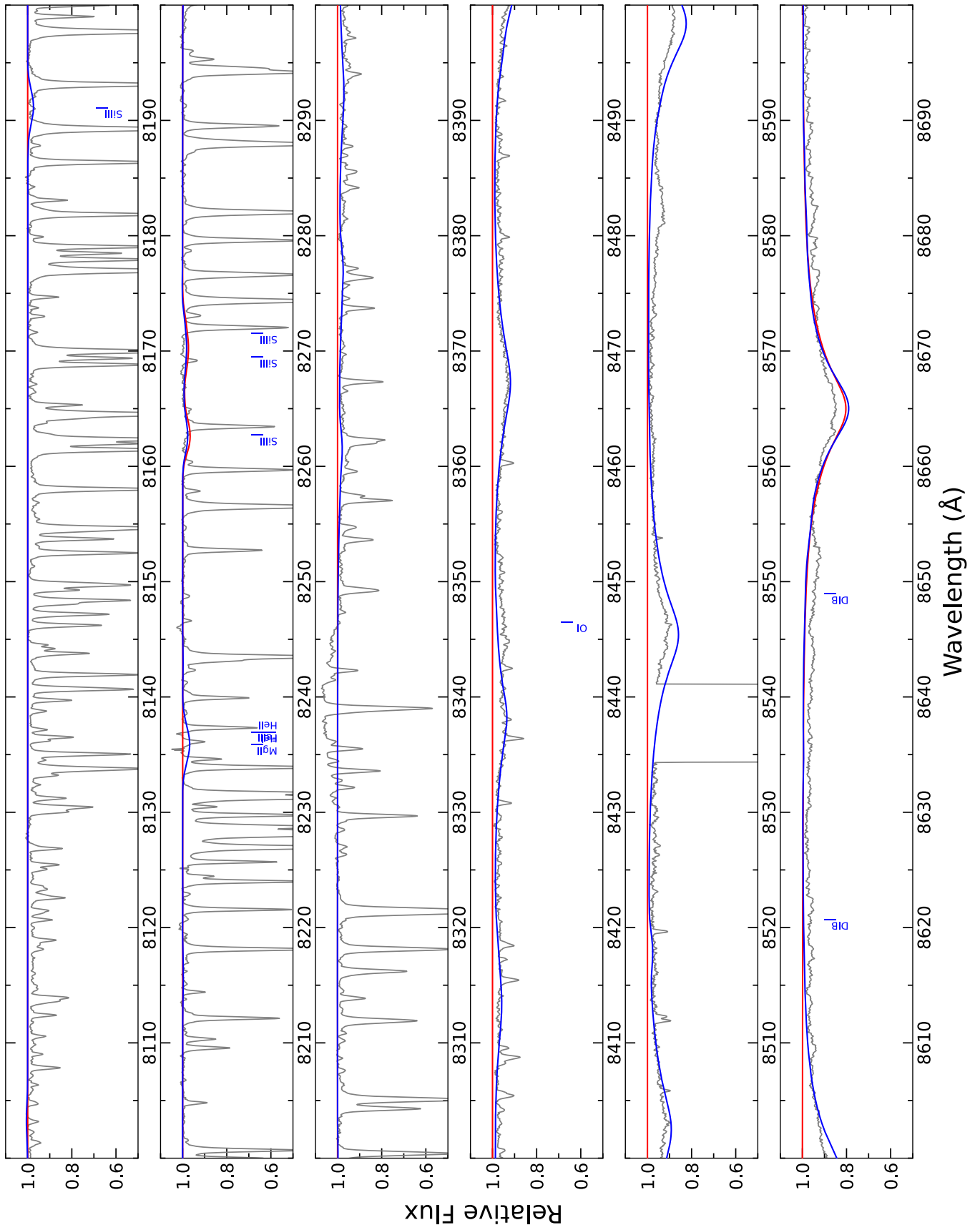


Fig. A.8. Same as Fig. A.1, but in the wavelength range 8100 to 8700 Å.

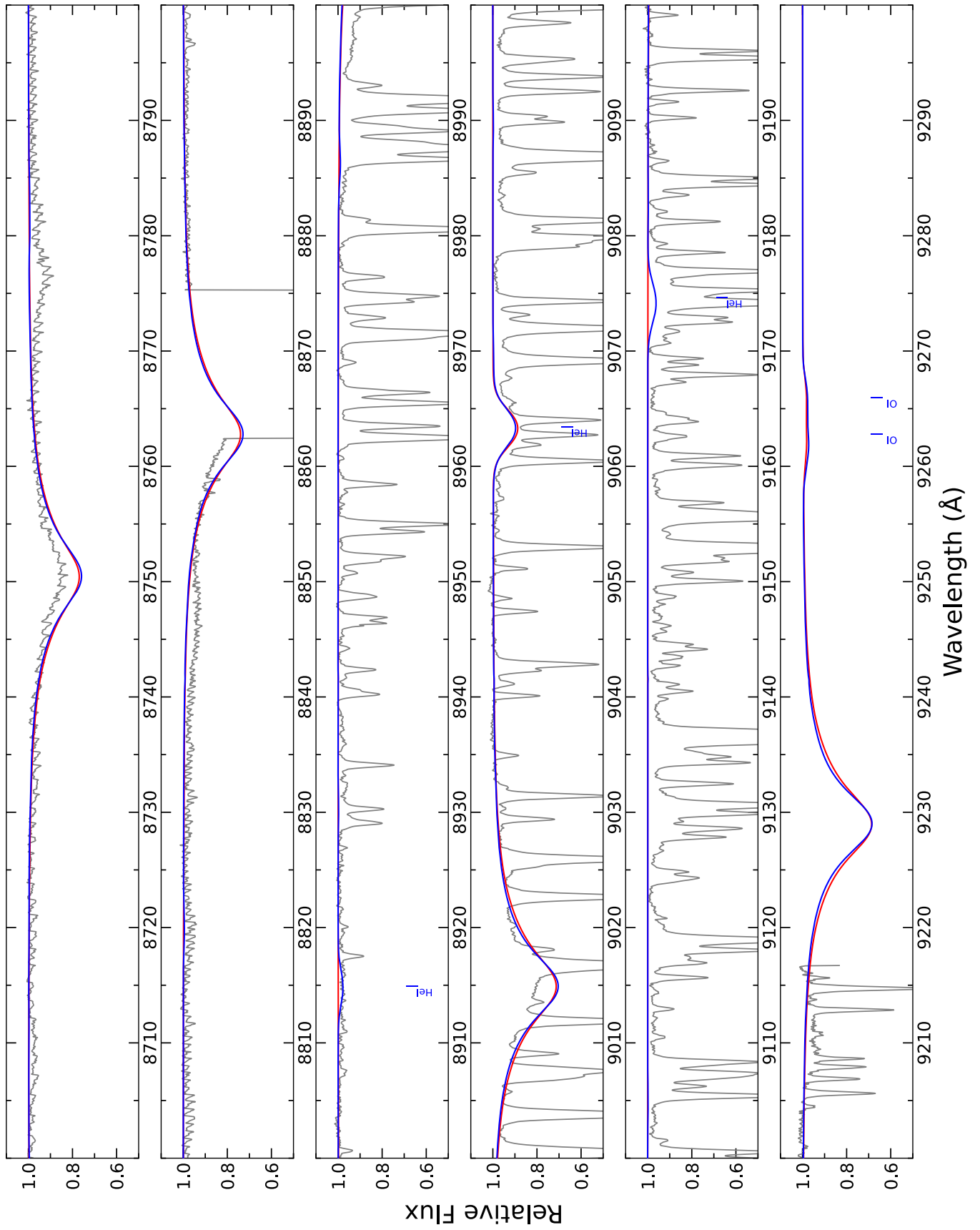


Fig. A.9. Same as Fig. A.1, but in the wavelength range 8700 to 9300 Å.

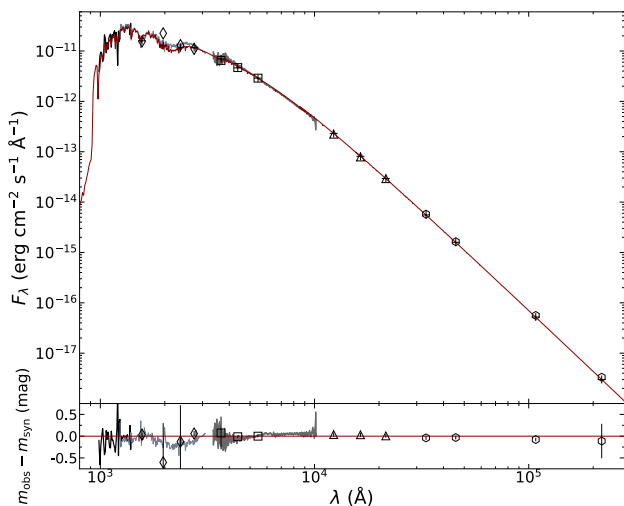


Fig. A.10. Spectral energy distribution of HD 93840. Upper panel: reddened ATLAS flux (solid red line) compared to various (spectro-) photometric measurements. Lower panel: difference between observed and modelled values in magnitudes. Spectrophotometric data of TUES, IUE, and *Gaia* are depicted as black, light gray, and dark gray lines, respectively. The photometric measurements are illustrated as follows: TD1 (diamonds), Johnson *UBV* (squares), 2MASS *JHK* (triangles) and AllWISE W1 to W4 photometric data (hexagons). The error bars in the lower panel represent the 2σ uncertainty ranges.

Table B.1. Distance effects on stellar parameters of HD 93840.

Parameter	Ads	FASTWIND
M_V (mag)	$-5.72^{+0.22}_{-0.21}$	$-6.38^{+0.33}_{-0.30}$
	$-5.18^{+0.46}_{-0.24}$	$-5.12^{+0.46}_{-0.23}$
	$-4.97^{+0.23}_{-0.25}$	$-4.91^{+0.23}_{-0.25}$
M_{bol} (mag)	$-7.75^{+0.23}_{-0.22}$	$-8.62^{+0.34}_{-0.30}$
	$-7.20^{+0.46}_{-0.55}$	$-7.36^{+0.46}_{-0.55}$
	$-7.00^{+0.24}_{-0.26}$	$-7.15^{+0.24}_{-0.26}$
M (M_\odot)	17.2 ± 0.8	22.1 ± 1.9
	$10.8^{+7.3}_{-3.9}$	$7.9^{+6.0}_{-3.1}$
	$8.9^{+2.8}_{-2.0}$	$6.5^{+2.8}_{-1.9}$
R (R_\odot)	22 ± 2	29 ± 5
	17^{+5}_{-3}	17^{+5}_{-3}
	16 ± 2	15 ± 2
$\log L/L_\odot$	5.00 ± 0.09	$5.34^{+0.12}_{-0.13}$
	$4.78^{+0.22}_{-0.19}$	$4.84^{+0.22}_{-0.19}$
	4.70 ± 0.10	4.76 ± 0.10

Notes. Values are given for the atmospheric parameters derived using Ads and FASTWIND, for three distances: $d_{\text{spec}} = 3740 \pm 340$ pc, $d_{\text{Gaia}}^{\text{MA}} = 2910^{+830}_{-550}$ pc and $d_{\text{Gaia}}^{\text{MA,EB}} = 2640^{+310}_{-250}$ pc (top to bottom).

of $d_{\text{Gaia}}^{\text{MA,EB}} = 2640^{+310}_{-250}$ pc from a Bayesian analysis using a prior from Maíz Apellániz et al. (2008) to describe the distribution of the OB star population. The corresponding posterior cumulative distance distribution (CDF) is displayed in the lower panel of Fig. B.1. The existence of a much larger parallax bias for relatively bright and blue stars like HD 93840 was proposed more recently by Maíz Apellániz (2022). Taking also into account the zero-point bias of Maíz-Apellániz we derive $d_{\text{Gaia}}^{\text{MA}} = 2910^{+830}_{-550}$ pc, again from a Bayesian analysis and stating 16th and 84th percentiles (see the lower panel of Fig. B.1, the flatter CDF). Both studies are solid within the assumptions made, the data adopted and the results obtained, consequently the distance to HD 93840 cannot be tightly constrained on the basis of the *Gaia* EDR3 parallax alone. We therefore consider both solutions in the fol-

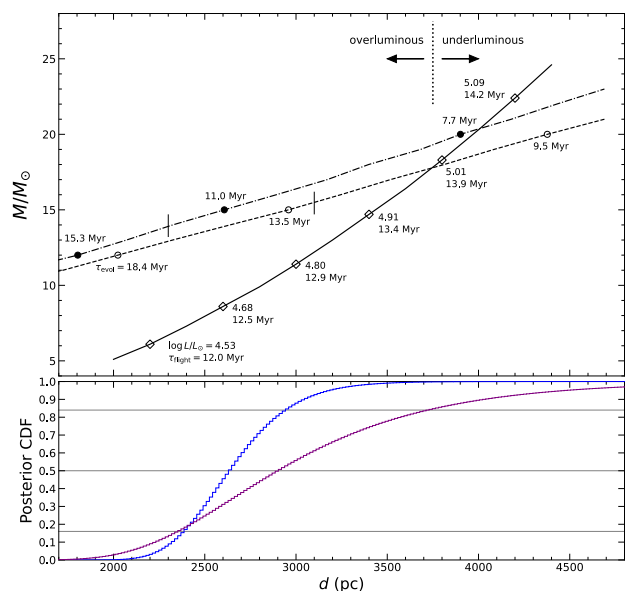


Fig. B.1. Upper panel: the full line follows the loci of stellar masses that reproduce the observed atmospheric parameters (Ads solution) of HD 93840 with distance as independent parameter, the dashed and dashed-dotted lines follow the loci where stellar evolution models of Ekström et al. (2012) show the same T_{eff} as HD 93840, for the rotating and non-rotating case, respectively. Values along the curves indicate luminosities and flight times τ_{flight} to reach the distance, adopting the kinematic parameters from Table 1 and assuming ejection from the disk mid-plane, or evolutionary timescales τ_{evol} for the models to reach T_{eff} of HD 93840. The vertical short lines indicate the points where $\tau_{\text{evol}} = \tau_{\text{flight}}$. The vertical dotted line marks d_{spec} , as the division line where HD 93840 would switch from being overluminous to becoming underluminous. Lower panel: posterior cumulative distance distributions (CDF) derived from a Bayesian approach, using the *Gaia* EDR3 parallax after application of the zero-point correction of Maíz Apellániz (2022), and assuming an uncertainty inflated according to El-Badry et al. (2021, blue CDF), and when considering parallax bias according to Maíz Apellániz (2022, purple CDF). The grey horizontal lines represent the 16th, 50th, and 84th percentile.

lowing. We note that both solutions roughly agree on a minimum distance of about 2.4 kpc. Moreover, $d_{\text{Gaia}}^{\text{MA,EB}}$ is in excellent agreement with the distance values provided by Bailer-Jones et al. (2021) and the inverted parallax value, despite the (slightly) inflated parallax uncertainty and the enhanced zero-point correction, which mutually have a compensating effect.

In order to attempt to constrain the distance to HD 93840 further, we investigated what consequences the derived distances have for the fundamental stellar parameter determination. Using the atmospheric parameters, extinction, and bolometric correction determined in the model atmosphere analysis, we derived a unique combination of luminosity, radius and mass per given distance value, all of which increase for increasing distance. Table B.1 shows some of the fundamental parameter values for our two quantitative spectroscopy solutions (Ads and FASTWIND), considering different characteristic distance values encountered before. The results for the stellar luminosity are visualised in the HRD in Fig. 1. We want to emphasise that the luminosity of HD 93840 would resemble that of a normally-evolving star only for d_{spec} . HD 93840 is overluminous for shorter distance values and underluminous for longer distances, with respect to a normally-evolving star of the same mass at the measured T_{eff} .

Further constraints on the distance to HD 93840 can be derived from the masses, and the associated stellar evolution times.

This is possible because of the runaway nature of the star, in that the flight time from the star-forming regions of the disk to the current position cannot be longer than the time for the star to evolve to its state in the HRD. While further details of the kinematic calculations in the Galactic potential are discussed in the Appendix C, we concentrate here already on the conclusions. One finds that the normally-evolving single-star scenario with HD 93840 located at d_{spec} can be dismissed. In fact, the range of potential masses can be constrained to below about 14 to $15.5 M_{\odot}$ (depending on initial rotational velocity) for normally-evolving single stars. This is a hard limit assuming dynamical ejection at birth, as H-burning constitutes the longest burning-phase in the stellar life. Overluminous stars in more advanced nuclear burning phases have shorter evolution times. This mass limit and the corresponding evolutionary age imply the distance to HD 93840 to be shorter than a hard limit of ~ 3.1 kpc.

However, one can push the constraints further. Assuming for example a current luminosity of $\log L/L_{\odot} = 4.68$ (for $d = 2.6$ kpc) to be an upper limit throughout the 12.5 Myr of time to reach its current position, one can calculate the total energy requirement to an equivalent of fusing about $5 M_{\odot}$ of hydrogen into helium, accounting for a $\sim 10\%$ additional contribution from 3α burning. As the luminosity likely increased with time, we may assume a mass of 3 to $4 M_{\odot}$ of H turned into He – plus about less than a Chandrasekhar mass of He-core⁵ from the sdO progenitor that has in the meantime been burnt into carbon – to be more realistic. We note that the luminosity of HD 93840 varies by a factor of less than two in the entire relevant distance range, such that the considerations above should be accurate to within better than $1 M_{\odot}$.

Furthermore, we can calculate the overluminosity of HD 93840 as a function of distance, which ranges from a factor over twenty for $d = 2.4$ kpc to slightly above two at $d = 3.1$ kpc, implying mean molecular weights (see Sect. 5) over the entire star of $\mu \approx 1.3$ to 0.7, respectively. The μ at the lower distance value would imply the star to consist almost entirely of helium and heavier elements, which seems unlikely, given the hydrogen-dominated atmosphere. On the other hand, one may calculate the mean molecular weight of the star given the constraints on the carbon core and He-masses above, plus adding mildly processed envelope material accreted from the former companion for the remainder of the total mass derived for a given distance. This provides values of μ between ~ 1.05 (for $d = 2.4$ kpc) and ~ 0.85 (for $d = 3.1$ kpc), which means too low values – compared to the global mean molecular weights from considering the overluminosities – at the short distance and too high values at the long distance limit. About consistent values are only obtained in the distance range between 2.6 to 2.8 kpc, which we finally adopt as the most likely distance range to HD 93840. This tight distance distribution is similar to those of the *Gaia*-based distances discussed above, except the one with uncertainties inflated according to Maíz Apellániz (2022). Interestingly, for a distance of 2.7 kpc the overluminosity of HD 93840 is a factor of seven, the average value found by Sen et al. (2022) for the overluminous components in binaries after interaction.

An independent confirmation of the distance to HD 93840 is nonetheless desirable. This has to await future *Gaia* data releases, when systematics will be better understood and statistical uncertainties will get reduced due to a longer baseline and larger number of measurements.

⁵ We can again use a lifetime argument here, a more massive He-core would not live long enough for the second mass transfer in the initial binary system to occur.

Appendix C: Kinematics

We employed the *Gaia* coordinates and proper motion components⁶, the *Gaia*-based $d_{\text{Gaia}}^{\text{MA,EB}}$ as discussed above and alternatively the 'long' d_{spec} , and the radial velocity as measured from the available spectroscopy as input data for the calculation of the Galactic orbit of HD 93840. The Galactic potential as described by Allen & Santillan (1991) and the code of Odenkirchen & Brosche (1992) were used for the numerical integration.

For the radial velocity determination in addition to the two FEROS spectra Phase 3 data of a further spectrum observed on 26 November 2013 with the Ultraviolet and Visual Echelle Spectrograph (UVES, Dekker et al. 2000) on the ESO Very Large Telescope (VLT) at Paranal in Chile were used. The blue ($R \approx 65\,000$) and red-arm ($R \approx 75\,000$) UVES spectra were investigated independently⁷. Each spectrum was investigated in two ways, i) by cross-correlation with the model spectrum, concentrating on spectral regions containing only metal lines, and ii) by analysing the Doppler shifts of >10 individual unblended metal lines per spectrum. This was done because the cores of the hydrogen lines – and to a lesser extent the helium lines – may be affected by the velocity field at the base of the (weak) stellar wind. This yielded a combined $v_{\text{rad}} = -8.1 \pm 0.5 \text{ km s}^{-1}$ (1σ standard deviation), as no significant change in radial velocity was found for the FEROS and UVES data, despite them having been taken more than eight years apart. We note that the highest accuracy and precision of the two spectrographs was not achieved, which would have required lamp frames to be taken adjacent to the science observations. A search of the literature on radial velocity measurements for HD 93840 provided only the work of Feast et al. (1955), who gave a value of $-2 \pm 4.5 \text{ km s}^{-1}$ from five measurements in the years 1952 and 1953. As supergiants show wind and also potentially pulsational variability – which have the potential to yield small radial velocity shifts –, and in view of the instrumental limitations in the 1950s it cannot be decided here whether the small difference between our value of v_{rad} and that of Feast et al. point to a SB1 nature of HD 93840, or not. We note, however, that such small differences have no significant effect on the orbit calculations. Nevertheless, radial velocity monitoring of the star is suggested to be undertaken in the future. Given the runaway nature of the star, and the radial velocity stability over the eight year span covered by modern instruments, a breakup of the former binary system appears more probable.

The kinematic study of HD 93840, visualised in Fig. 3, yields values of the galactocentric Cartesian velocity components in radial and Galactic rotation direction, and perpendicular to the Galactic plane towards the Galactic north pole, $U = -83 \text{ km s}^{-1}$, $V = 225 \text{ km s}^{-1}$, and $W = 28 \text{ km s}^{-1}$, respectively. The orbital motion brought HD 93840 already more than 500 pc above the Galactic mid-plane, which corresponds to about ten scale heights of the typical OB star population⁸. Other stars from our previous work show similar trajectories, as visualised in Fig. 3.

⁶ The *Gaia* EDR3 proper motions were corrected for magnitude-dependent systematics according to Cantat-Gaudin & Brandt (2021), which turned out to be below the percent level for HD 93840.

⁷ We note that the UVES data was dropped from the quantitative spectral analysis because of the much lower S/N than obtained in the combined FEROS spectrum.

⁸ The scale height of the OB star population is small, in the range of about 35 to 70 pc (see e.g. Maíz-Apellániz 2001, and references therein), compared to scale heights of other stellar populations of the Galactic disk. The scale height for the intermediate-age A-F-type star population (≤ 2 Gyr) is 150 to 200 pc (see e.g. Mackereth et al. 2017), whereas the scale height of the old thin-disk star population is usually discussed in the literature to be about 300 pc, and more. The supergiant

These are the two ON stars with a binary history, HD 14633 and HD 201345 from [Aschenbrenner et al. \(2023\)](#), and HD 91316 (ρ Leo), a likely eccentric binary from Paper II, probably ejected dynamically. The supergiant HD 93840 shows the most pronounced CNO mixing signature among these, well beyond the values of the two main-sequence ON stars.

HD 93840 is found far from the usual location of massive stars. From the study of the OB star population distribution one also finds that the Sun is located about 10 to 25 pc above the Galactic mid-plane, see also e.g. [Maíz-Apellániz \(2001\)](#), and references therein).